Iterative image reconstruction for CBCT using edge-preserving prior

Jing Wang
Department of Radiation Oncology, Stanford University School of Medicine, Stanford, California 94305

Tianfang Li
Department of Radiation Oncology, University of Pittsburgh Cancer Institute, Pittsburgh, Pennsylvania 15901

Lei Xing[a)]
Department of Radiation Oncology, Stanford University School of Medicine, Stanford, California 94305

On-board cone-beam computed tomography (CBCT) is a new imaging technique for radiation therapy guidance, which provides volumetric information of a patient at treatment position. CBCT improves the setup accuracy and may be used for dose reconstruction. However, there is great concern that the repeated use of CBCT during a treatment course delivers too much of an extra dose to the patient. To reduce the CBCT dose, one needs to lower the total mAs of the x-ray tube current, which usually leads to reduced image quality. Our goal of this work is to develop an effective method that enables one to achieve a clinically acceptable CBCT image with as low as possible mAs without compromising quality. An iterative image reconstruction algorithm based on a penalized weighted least-squares (PWLS) principle was developed for this purpose. To preserve edges in the reconstructed images, we designed an anisotropic penalty term of a quadratic form. The algorithm was evaluated with a CT quality assurance phantom and an anthropomorphic head phantom. Compared with conventional isotropic penalty, the PWLS image reconstruction algorithm with anisotropic penalty shows better resolution preservation. © *2009 American Association of Physicists in Medicine.* [DOI: 10.1118/1.3036112]

I. INTRODUCTION

Integration of the cone-beam computed tomography (CBCT) with a linear accelerator[1] makes it possible to acquire volumetric image of high spatial resolution for a patient at treatment position. There is growing interest in using on-board CBCT for patient setup and dose reconstruction.[2] Repeated use of CBCT during a treatment course has raised concern of the extra radiation dose delivered to patients.[3,4] One cost-effective way to reduce the CBCT dose is to acquire CT with a lower mAs protocol. However, image quality will degrade dramatically due to excessive noise,[5,6] rendering the low-mAs CBCT a less attractive option for the therapeutic guidance.

In this work, we incorporate the noise properties of CBCT log-transformed projection data[7,8] in a statistical iterative image reconstruction algorithm to improve the low-dose CBCT image quality. Compared with analytical reconstruction algorithms, a major advantage of iterative algorithms is that it takes into consideration the image physics, noise properties, and imaging geometry elegantly. Advantages of iterative reconstruction algorithms have been demonstrated in the image reconstruction of emission tomographic images.[9–12] However, when applying iterative reconstruction algorithms for CT imaging,[13–17] long computational time may pose a challenge for their clinical applications. With the development of fast computers and dedicated hardwares,[18,19] iterative reconstruction algorithms may be used for clinical CT reconstruc-

tion in the near future. Recently, iterative image reconstruction algorithms have demonstrated superior performance for reconstruction of the multislice helical CT (Ref. 20) and cardiac micro-CT.[21] Prototype products based on iterative reconstruction methods have been exhibited by major CT vendors in a number of national and international meetings.

In statistics-based iterative reconstruction algorithms, tomographic images are reconstructed by minimizing or maximizing a cost function, which is constructed based on noise characteristics of the measured data. There are usually two terms in the objective function. The first term models the statistics of measured data and the second term reflects *a prior* information to regularize the solution. Many efforts[7,22] have been devoted to investigate the noise models of the measurements in CT. Accurate noise modeling is a prerequisite of a statistical iterative reconstruction algorithm. The second term, i.e., the regularization term, also plays an important role for successful image reconstruction. One common choice of the regularization term is the Gaussian Markov random field in quadratic form.[16,23–25] Such quadratic penalty with equal weights for neighbors of equal distance encourages equivalence between neighbors without considering discontinuities in images, which may lead to over-smoothing around edges or boundaries. Several edge-preserving regularization methods have been proposed to address this problem. For example, the edge-preserving Huber penalty, which penalizes neighbors of small differences quadratically while applying a linear penalty on neighbors of

larger difference, has been used by Elbakri and Fessler[26] for CT image reconstruction and by Chlewicki *et al.*[27] for positron emission tomography reconstruction. A line process has been introduced by Geman and Geman[28] to define the edge lattice during Bayesian restoration of images. Geman and Reynolds[29] proposed a finite asymptotic edge-preserving function and Charbonnier *et al.*[30] introduced an auxiliary variable in the prior constraint to mark the discontinuities in the images. These modifications make the objective function nonquadratic and complicate the computation. In this work, we propose a quadratic regularization term with anisotropic weights for different neighbors. The role of the anisotropic penalty is to discourage the equivalence between neighbors if the gradient is large; thus the edges or discontinuities will be better preserved in the final reconstructed image.

In the following sections, we first introduce the penalized weighted least squares (PWLS) objective function for image reconstruction of CBCT based on the noise properties of CBCT projection data. We then describe the proposed anisotropic penalty in details. In Sec. III, the evaluation of the proposed algorithm is presented using a quality assurance phantom and an anthropomorphic head phantom, followed by the discussion in Sec. IV and the conclusion in Sec. V.

II. METHODS AND MATERIALS

II.A. PWLS image reconstruction

Noise in x-ray CT projection data after logarithm transform follows approximately Gaussian distribution and the variance of the noise can be determined by an exponential formula[7,8]

$$\sigma_i^2 = \exp(\bar{p}_i)/N_{i0}, \tag{1}$$

where N_{i0} is the incident photon number at detector bin i, $\bar{p}_i$ and σ_i^2 is the mean and variance of projection datum p_i, respectively. Based on the noise properties of CT projection data, the PWLS cost function in the image domain can be written as

$$\Phi(\mu) = (\hat{p} - A\mu)'\Sigma^{-1}(\hat{p} - A\mu) + \beta R(\mu). \tag{2}$$

The first term in Eq. (2) is the weighted least-squares criterion, where $\hat{p}$ is the vector of log-transformed projection measurements, and μ is the vector of attenuation coefficients to be reconstructed. Operator A represents the system or projection matrix. The element of a_{ij} is the length of the intersection of projection ray i with pixel j and it is calculated by a fast ray-tracing technique.[31] In our implementation, the element of matrix A was precomputed, stored as a file, and used as a lookup table later. The projection data $\hat{p}$ and the attenuation map μ is related by $\hat{p}=A\mu$. Σ is a diagonal matrix with the ith element of σ_i^2, i.e., an estimate of the variance of measured $\hat{y}_i$ at detector bin i which can be estimated from the measured projection data according to Eq. (1). The element of the diagonal matrix plays the role of weighting in the WLS cost function and it determines contribution of each measurement. The symbol $'$ denotes the transpose operator. The second term in Eq. (2) is a smoothness penalty or a prior constraint, where β is the smoothing or penalty parameter

which controls relative contribution from the measurement and prior constraint. The image reconstruction task is to find attenuation map μ by minimizing the objective function (2) with a positive constraint. The Gaussian–Seidel updating strategy was used for the minimization and details about the implementation are described in the Appendix.

II.B. Edge-preserving anisotropic penalty

The prior constraint in Eq. (2) enforces a roughness penalty on the solution. The quadratic penalty with equal weights for neighbors of the same distance has been used widely for iterative image reconstruction[16,17,23,25]

$$R(\mu) = \mu'R\mu = \frac{1}{2}\sum_j \sum_{m \in N_j} w_{jm}(\mu_j - \mu_m)^2, \tag{3}$$

where index j runs over all image elements in the image domain, N_j represents the set of neighbors of the jth image pixel. The parameter w_{jm} was set to 1 for first-order neighbors and $1/\sqrt{2}$ for second-order neighbors in previous applications.[17,23,25] This type of penalty only takes distance information of the neighbors into account. That is, the neighbors of the same distance play an equivalent role in regularizing the solution, and *vise versa*. A major shortcoming of the approach is that the regularization does not take the difference in intensities of the neighboring voxels (e.g., edges or discontinuities) into account, which may lead to an oversmoothed solution for reconstructed images. To overcome this limitation, we propose an anisotropic penalty to regularize the solution. In this formulation, the weight is smaller if the difference between a neighbor and the concerned voxel is larger, since the coupling between two such neighbors is smaller. There are many choices that satisfy this behavior of weighting. In this work, we chose the form of w_{jm} to be the same as the conduction coefficient in the well-known anisotropic diffusion filter.[32] The weight w_{jm} can be written as

$$w'_{jm} = w_{jm} \exp\left[-\left(\frac{\mu_j - \mu_m}{\delta}\right)^2\right], \tag{4}$$

where the gradient and the parameter δ determine the strength of the diffusion during each iteration. The parameter δ can be set either by hand or to the value at 90% of the histogram of the gradient magnitude of the image to be processed. In this work, we set the value of δ to be 90% of the histogram of the gradient magnitude of the FDK reconstructed image (which is used as the initial during iterative reconstruction).

II.C. CBCT data acquisition

Cone-beam CT projection data were acquired by an Acuity simulator (Varian Medical Systems, Palo Alto, CA). The number of projections for a full 360° rotation is 680 and the total time for the acquisition of one full circle of the projection data is about 1 min. The dimension of each acquired projection image is 397 mm × 298 mm, containing 1024 × 768 pixels. To save computational time during iterative reconstruction, the projection data at each projection view
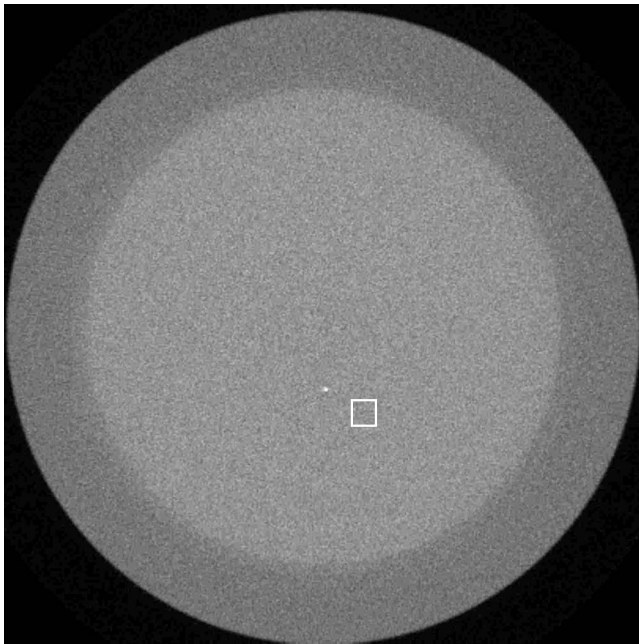
FIG. 1. The bead point object in the CatPhan® 600 phantom was used to calculate the MTF of reconstructed images. Display window: $[0,0.03]$ mm^{-1}. The white square in the image indicates the region used to calculate the standard deviation.

were downsampled by a factor of 2 and only 16 out of 768 projection data along the axial direction were chosen for reconstruction. The system has a field of view of 25 cm $\times$ 25 cm (full-fan mode) in the transverse plane and 17 cm in the longitudinal direction, which can be increased to 45 cm $\times$ 45 cm in the transverse plane by shifting the detector laterally (half-fan mode).

Two phantoms were used to evaluate the performance of the proposed PWLS algorithm. The first is a commercial calibration phantom CatPhan® 600 (The Phantom Laboratory, Inc., Salem, NY). The second is an anthropomorphic head phantom. In both phantom studies, the tube voltage was set to 125 kVp. The x-ray tube current was set at 10 mA and the duration of the x-ray pulse at each projection view was 10 ms during the acquisition of low-dose CBCT projection data. During acquisition of the corresponding high-dose CBCT image, the tube current was set at 80 mA and the duration of the x-ray pulse was set at 12 ms. The projection data were acquired in full-fan mode and the full-fan bow-tie filter was used for both phantoms. The distance of source-to-axis is 100 cm and source-to-detector distance of 150 cm. The size of reconstructed image is $350 \times 350 \times 16$ and voxel size is $0.776 \times 0.776 \times 0.776$ mm^3.

II.D. Performance evaluation

We used the CatPhan® 600 phantom to study the spatial resolution of images reconstructed by different algorithms. The CTP591 module of the CatPhan® 600 phantom contains a bead point object with a diameter of 0.28 mm (see Fig. 1). The point object can be used to calculate the modulation transfer function (MTF) which characterizes the spatial res-
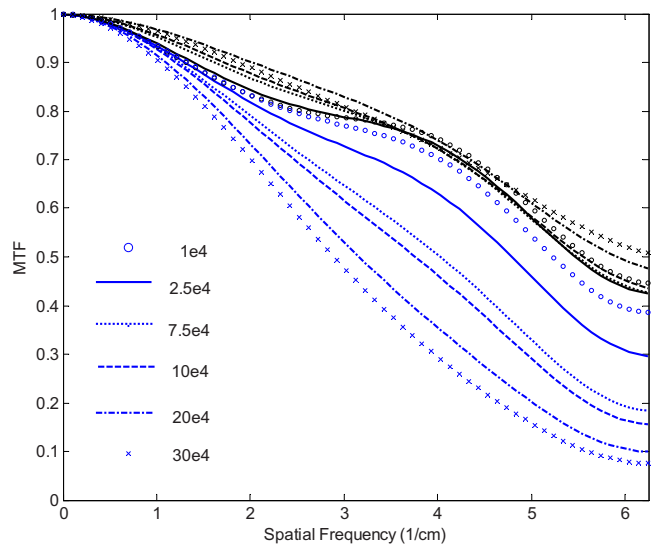

FIG. 2. MTF curves of two PWLS iterative image reconstruction algorithms with different smoothing parameters. Curves in the blue color are results of reconstruction using an isotropic quadratic penalty. Curves in the black color are results of reconstruction using the edge-preserving anisotropic quadratic penalty.

olution of images. The reconstructed image contains the point object provides the point-spread-function for each reconstruction algorithm and the in-plane MTF can be obtained by calculating two-dimension Fourier transform and averaging over 2π angles. A 10×10 matrix centered about the point object was used to calculate the MTF after the background value (which can be estimated by averaging the values of a uniform background region) was subtracted from the value of each pixel.

In the CTP404 module of the CatPhan® 600, there are several circles of different intensities which can be used to quantify the contrast-to-noise (CNR) of the reconstructed images in different reconstructions. We selected a low-contrast region of interest (ROI) for calculation of the CNR in the image reconstructed by different algorithms since a low-contrast region is of interest in CT imaging. The contrast was calculated as the absolute difference between the mean value of the region inside the ROI and the mean value of the uniform background region. The noise level was characterized by the standard deviation of a uniform area of size 15 pixels by 15 pixels. The CNR was defined as the contrast divided by the standard deviation.

III. RESULTS

III.A. CatPhan® 600 phantom

III.A.1. MTF measurement

Figure 2 shows the MTFs of two iterative reconstruction algorithms with different smoothing parameters β ranging from 1.0×10^4 to 30×10^4. It can be observed that the spatial resolution of the reconstructed image using an isotropic quadratic penalty decreases as smoothing strength increases. The frequency of 50% MTF for the iterative reconstruction using the isotropic penalty decreases from 5.25 to 2.91 1/cm as
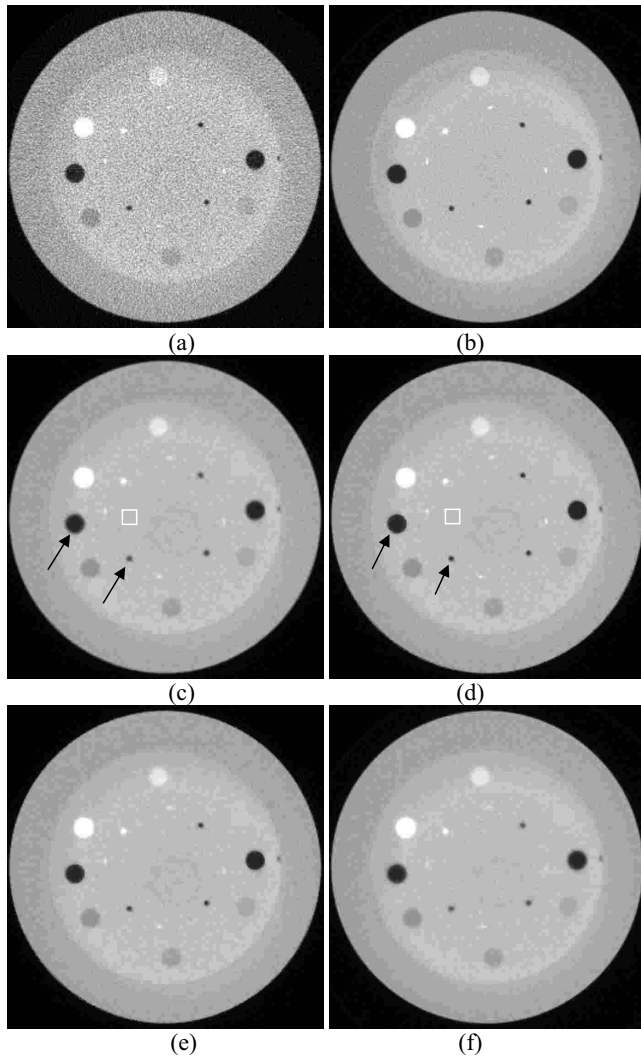
FIG. 3. CBCT of the CatPhan® 600 phantom: (a) analytical FDK reconstructed image from projection data acquired using a low-dose protocol (10 mA/10 ms) and (b) a high-dose protocol (80 mA/12 ms); (c) PWLS iterative image reconstruction with the isotropic quadratic penalty from projection data acquired using a low-dose protocol and (d) with the proposed anisotropic penalty; (e) PWLS iterative image reconstruction with the Huber penalty; (f) analytical FDK reconstructed image after low-dose projection data processed by the PWLS criterion (Ref. 34) with a smoothing parameter of 0.09. Display window: [0,0.02] mm^{-1}.

the smoothing parameter increases from 1.0×10^4 to 30×10^4. In contrast, MTF curves of the image reconstructed using the proposed edge-preserving anisotropic quadratic penalty are clustered together with various smoothing parameters. This indicates that the spatial resolution in images reconstructed using the anisotropic quadratic penalty is better-preserved.

### III.A.2. Full width at half maximum measurement

We then tested the proposed algorithm on the CTP404 module of the CatPhan® 600 phantom. A representative slice of the CBCT images obtained by different reconstruction methods are shown in Fig. 3. Figure 3(a) is the low-dose image reconstructed by analytical FDK algorithm. It can be

observed that noise level is high in this low-dose CBCT image. Figure 3(c) shows the image reconstructed by the PWLS algorithm using the isotropic quadratic penalty with the penalty parameter $\beta = 30 \times 10^4$. Figure 3(d) displays the image reconstructed by the PWLS algorithm using the proposed edge-preserving anisotropic penalty with the same penalty parameter. The noise in the images reconstructed by iterative algorithms is greatly suppressed compared with the image reconstructed using the analytical method. It is seen that the edges were blurred in Fig. 3(c), as indicated by the arrows in the image. This is not surprising since an isotropic quadratic form penalty simply encourages equivalence among neighbors along all directions without considering the boundary information presented in the image. However, edges were well preserved when the anisotropic penalty was used as the constraint (see the corresponding area in Fig. 3(d) indicated by the arrows).

To quantitatively analyze the gain by using the anisotropic penalty in the iterative reconstruction algorithm, we then studied the full-width-at-half-maximum (FWHM) of two pointlike objects (one is brighter than background and the other one is darker than the background) in the reconstructed images. Figure 4 shows the profiles passing through two pointlike objects in Figs. 3(c) and 3(d). Through those profiles, it can be observed that the major difference between the solutions using isotropic and anisotropic penalties is nearby edges. The intensity values in both images at a uniform region are nearly identical; see line along value 0.016 in both Figs. 4(a) and 4(b). It can also be observed in Fig. 4 that the peak of the profile from the image reconstructed using the isotropic quadratic penalty is lower than that from the reconstructed image using the anisotropic penalty, while the bottom of the profile from the image reconstructed using the isotropic quadratic penalty is higher than that from the reconstructed image using anisotropic penalty. These observations show that there is a signal loss when an image is reconstructed by the PWLS algorithm using the isotropic penalty. The standard deviation of a uniform region (indicated by a white square) is 0.50×10^{-3} in Fig. 3(c) and 0.54×10^{-3} in Fig. 3(d). We then fitted the profile to a Gaussian functional. The FWHM of brighter source is 3.48 pixels for the image reconstructed with the isotropic penalty and 3.19 pixels for the anisotropic penalty. The FWHM for the darker source is 3.71 pixels for the image reconstructed with the isotropic penalty and 3.48 pixels for the anisotropic penalty. In both cases, better edge preserving was observed in the image reconstructed using the anisotropic penalty.

III.A.3. CNR measurement

Table I lists the CNR of two iterative reconstruction algorithms with different smoothing parameters. It can be observed that in both reconstruction algorithms the CNR increase as smoothing parameter increases. The CNR of the image reconstructed using the anisotropic penalty is slightly larger than that of the isotropic penalty when the same smoothing parameters are used. However, at the matched resolution between the two methods, CNR was increased
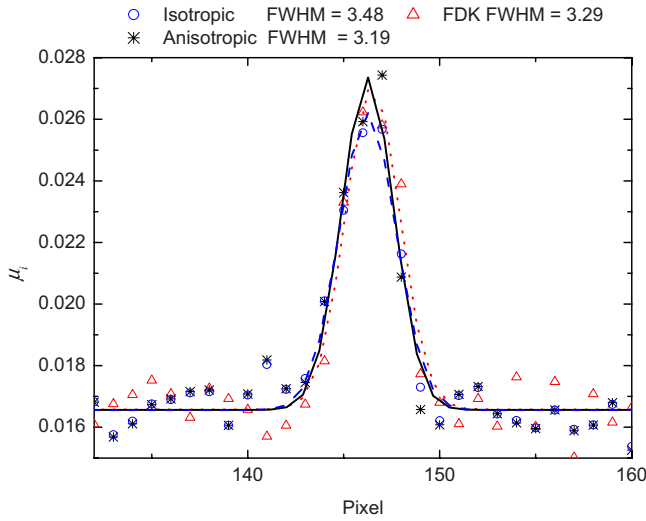
(a)
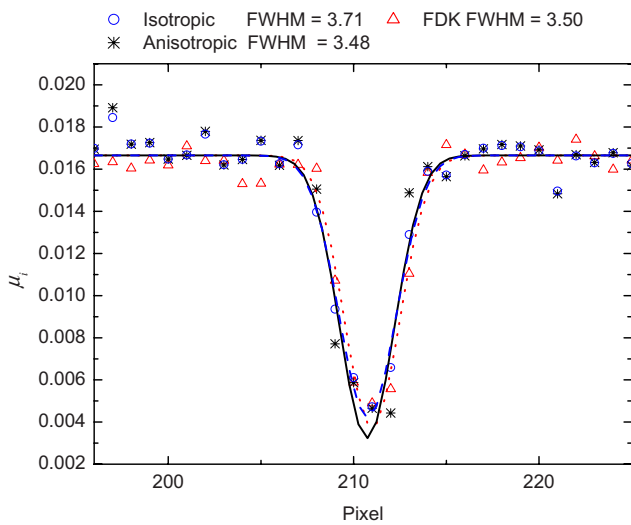
(b)

FIG. 4. Vertical profile through column 139 in Figs. 3(c) and 3(d). (a) shows the profile through the hot spot and (b) shows the profile through the cold spot. Edges are better preserved by using the anisotropic penalty as measured by the FWHM.

from 0.84 in the image reconstructed using the isotropic penalty with $\beta = 1.0 \times 10^4$ to 2.83 in the image reconstructed using the anisotropic penalty with $\beta = 30 \times 10^4$.

III.A.4. Comparison study with the Huber penalty

In this section, we compared the proposed anisotropic quadratic penalty with a representative edge-preserving non-quadratic penalty: the Huber penalty.[26,27] The Huber penalty function has the following form:

TABLE I. CNRs of the low-contrast ROI in Fig. 3.

$\beta \ (\times 10^4)$	1	2.5	7.5	10	20	30
PWLS isotropic	0.84	0.98	1.40	1.60	2.35	3.01
PWLS anisotropic	0.77	0.82	1.04	1.20	2.22	2.83
FDK (10 mA/10 ms)			0.95			
FDK (80 mA/12 ms)			2.66			

$$H(t) = \begin{cases} t^2/2, & |t| < \theta \\ \theta(|t| - \theta) + \theta^2/2, & |t| \geq \theta. \end{cases} \quad (5)$$

The Huber function penalizes the difference between neighboring pixels quadratically if the absolute difference pixel value $|t|$ is smaller than some threshold θ and it will apply a linear penalty to the larger differences of $|t| \geq \theta$ which usually occur at edges.

Figure 3(e) shows the PWLS reconstructed CatPhan® 600 phantom by using the Huber penalty with threshold $\theta = 0.001$ and the penalty parameter $\beta = 35 \times 10^4$. It can be observed that the edges are better preserved in the images reconstructed using the Huber penalty than the images reconstructed by using the isotropic quadratic penalty. To quantitatively compare the performance of the Huber penalty and the anisotropic quadratic penalty, we calculated the MTF of the CTP591 module of the CatPhan® 600 phantom at matched noise level. Figure 5 shows the MTF curves from the proposed anisotropic quadratic penalty with penalty parameter $\beta = 30 \times 10^4$ and the Huber penalty with threshold $\theta = 0.001$. The penalty parameter β in the PWLS reconstruction with Huber penalty was set at 35×10^4 so that the noise level in the reconstructed image is matched to the anisotropic quadratic penalty. The standard deviation of the uniform region (indicated by a white square in Fig. 1) in the image reconstructed using the Huber penalty is 0.73×10^{-3} and is 0.70×10^{-3} in the image reconstructed using the anisotropic quadratic penalty. MTF curves in Fig. 5 show that the aniso-
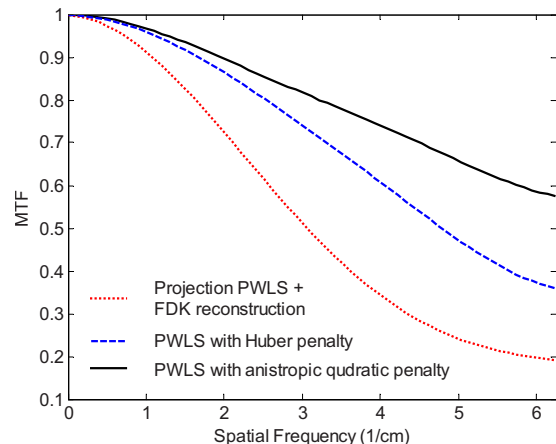

FIG. 5. MTF curves of the low-dose CBCT image reconstructed by different algorithms at a match noise level.
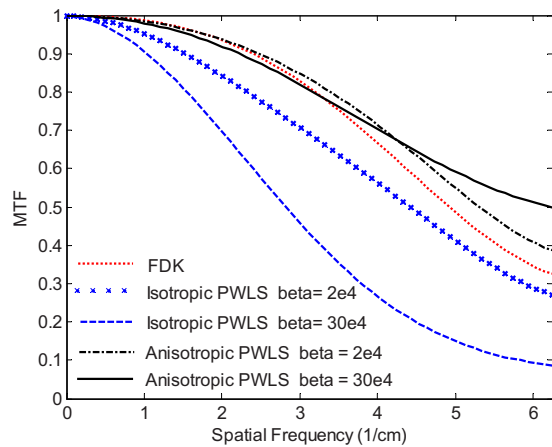
FIG. 6. MTF curves of the high-dose CBCT image reconstructed by different algorithms.

tropic quadratic penalty produces better image resolution at the matched noise level. The advantage of the anisotropic quadratic penalty may be attributed to that the Huber function depends on a hard threshold of the gradient while the anisotropic quadratic penalty considers the gradient information continuously by introducing Eq. (4).

III.A.5. Comparison with high-dose CBCT

For the projection data acquired with a tube current of 80 mA and x-ray pulse duration of 12 ms protocol, we reconstructed the CBCT image using the analytical FDK algorithm. We first compared the MTF of the image reconstructed by the analytical FDK algorithm with the image reconstructed by iterative PWLS algorithms at a matched noise level. The standard deviation of the uniform area is 5.95×10^{-4} in the FDK-reconstructed image. By setting the smoothing parameter $\beta = 2 \times 10^4$, the standard deviation of the same region in the PWLS-reconstructed image is 5.96×10^{-4} with the isotropic penalty and 5.98×10^{-4} with the anisotropic penalty. Figure 6 shows the MTF curves from the image reconstructed by FDK and the iterative PWLS algorithms. It can be observed that the MTF of the PWLS algorithm with the anisotropic penalty is slightly better than that of the FDK algorithm, whereas the MTF of the FDK algorithm is better than that of the PWLS algorithm with isotropic penalty. This demonstrates that better spatial resolution is achieved by the PWLS algorithm using the proposed edge-preserving anisotropic penalty. The same trend can also be seen from the profiles through the pointlike objects in the CTP404 module (Fig. 4). The FWHM obtained from the fitted Gaussian function also shows that better spatial resolution is achieved by using the PWLS image reconstruction algorithm with the anisotropic penalty.

From Table I, it is seen that the CNR of the PWLS reconstructed low-dose image using the anisotropic penalty with the penalty parameter $\beta = 30 \times 10^4$ is 2.83, which is slightly higher than that of the FDK reconstructed high-dose

image—2.66. In Fig. 6, we also show the MTF curve of the PWLS algorithm using the anisotropic penalty with the penalty parameter $\beta = 30 \times 10^4$. It can be observed that the MTF of the PWLS algorithm with the anisotropic penalty is comparable to that of the FDK algorithm. This result suggests that the PWLS iterative image reconstruction with the anisotropic penalty is capable of producing images with a CNR comparable to FDK-reconstructed high-dose images using only about $1/10$ dose without sacrificing image spatial resolution.

III.B. Anthropomorphic head phantom

Results of the anthropomorphic head phantom are shown in Fig. 7. Figure 7(a) shows one slice of the image reconstructed by the analytical FDK algorithm from projection data acquired using a low-dose protocol (10 mA/10 ms); Fig. 7(b) is the FDK reconstructed image for the same phantom acquired with a high-dose protocol (80 mA/12 ms). Figure 7(c) shows the same slice of a low-dose CBCT image reconstructed by the PWLS iterative algorithm using the isotropic penalty with the penalty parameter of $\beta = 30 \times 10^4$ and Fig. 7(d) shows the low-dose CBCT image reconstructed by the PWLS image reconstruction algorithm using the anisotropic penalty with the same penalty parameter. Figure 7(e) shows the PWLS reconstructed low-dose CBCT image using the edge-preserving Huber penalty with threshold $\theta = 0.001$ and the penalty parameter $\beta = 35 \times 10^4$. It can be observed that noise in low-dose CT images is efficiently suppressed in images reconstructed by the PWLS iterative reconstruction algorithms. The quality of low-dose CBCT reconstructed by the PWLS with anisotropic penalty is comparable to that of the high-dose FDK reconstructed image. With the anisotropic penalty in the PWLS iterative reconstruction, edges are better preserved in the reconstructed image. In the regions indicated by arrows in Fig. 7(d), it is seen that the structure is well preserved in the image reconstructed using the anisotropically penalized PWLS algorithm. The structure is blurred if the isotropic penalty was used during the PWLS reconstruction. This observation is consistent with the quantitative evaluation using the CatPhan® 600 phantom.

IV. DISCUSSION

The weighted least-squares criterion reflects that the measured data with a lower SNR will contribute less to the estimation of the attenuation map. The PWLS objective function is equivalent to the penalized maximum likelihood or maximum *a posteriori* criterion for Gaussian distributed noise. This is consistent with the observations from repeated measurements of x-ray CT projection data after logarithm transform.[7,8] The PWLS criterion for the CT projection data can also be derived from Poisson noise model of detector counts using the second-order Taylor expansion.[16] Measurement of x-ray counts can be modeled more accurately using the compound Poisson noise of polyenergetic x-ray beam
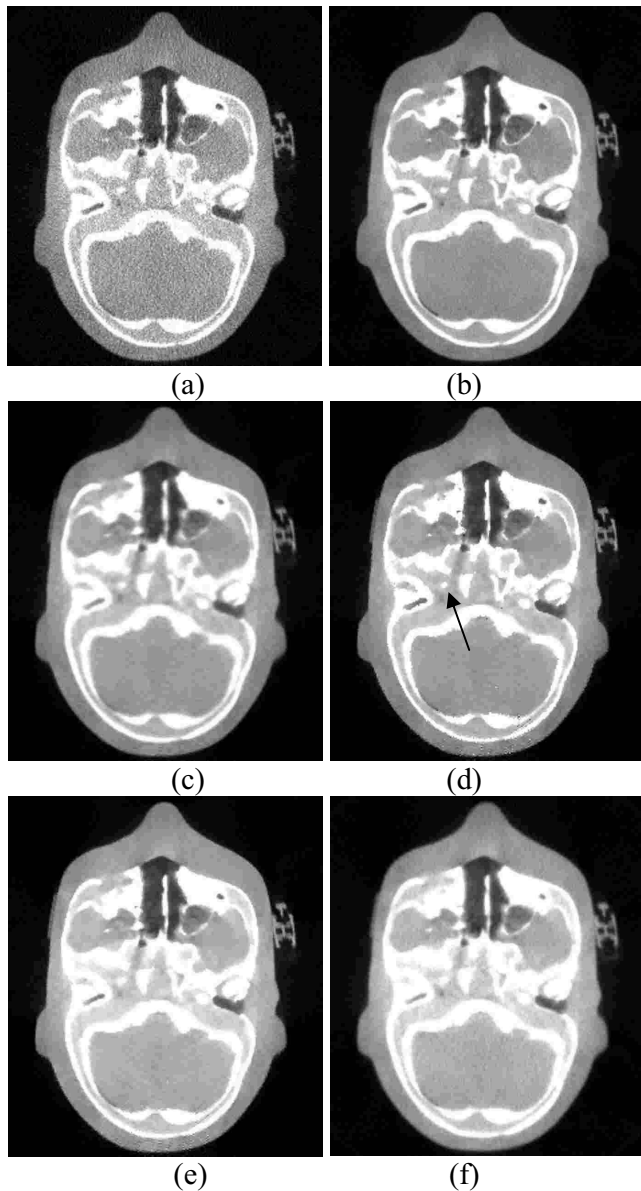
FIG. 7. CBCT of the anthropomorphic head phantom: (a) analytical FDK reconstructed image from projection data acquired using a low-dose protocol (10 mA/10 ms) and (b) a high-dose protocol (80 mA/12 ms); (c) PWLS iterative image reconstruction with an isotropic quadratic penalty from projection data acquired using a low-dose protocol and (d) with a proposed anisotropic penalty. (e) PWLS iterative image reconstruction with the Huber penalty; (f) analytical FDK reconstructed image after low-dose projection data processed by the PWLS criterion (Ref. 34) with smoothing parameter 0.09. Display window: $[0,0.02]$ mm^{-1}.

plus Gaussian electronic noise.[22] The performance of iterative reconstruction algorithms for x-ray CT may be further improved by more accurate noise modeling.

The penalty reflects the prior information of the CT images. In this work, the anisotropic penalty of the quadratic form was proposed to encourage smoothness among neighboring pixels of similar intensities but discourage the smoothness if a large difference exists between neighboring pixels. Thus, edges are better preserved in reconstructed images. In radiotherapy, CT images of the same patient are

usually available before treatment. The high-quality planning CT images provide strong *a priori* information of the patient and it may be used to improve the performance of iterative image reconstruction algorithms. However, interfractional variation in treatment position and deformation of organs may make such application challenging. Dedicated registration algorithms[33] are necessary to extract information from the planning CT as a prior constraint for iterative reconstruction.

Based on the same noise properties of projection data, the PWLS objective function can also be constructed in the projection or sinogram domain where the penalty is applied between neighboring projection pixels.[34] CT images can then be reconstructed by analytical algorithms such as FDK. Compared with fully iterative image reconstruction methods, the strategy of projection smoothing followed by analytical image reconstruction is advantageous in computational efficiency because projection and backprojection cycles in the iterative image reconstruction algorithm are avoided. Recently, La Riviere and Vargas[35] have shown potential equivalence between the image-domain based iterative reconstruction methods and the strategy of sinogram restoration plus analytical filtered backprojection reconstruction. The studies performed in their work[35] are based on a simple isotropic quadratic penalty. It will be interesting to perform a similar study based on the proposed anisotropic quadratic penalty. The edge-preserving penalty in image domain may have some advantages compared with the same penalty used in projection domain because edges are better defined in the image domain than of that in the projection domain. In this work, we also included the results obtained using the strategy presented in Ref. 34, i.e., the projection image is processed according to the PWLS criterion before the analytical FDK reconstruction. Figures 3(f) and 7(f) show the results from the projection-domain approach[34] with smoothing parameter $\beta=0.09$ for the CatPhan® 600 phantom and the anthropomorphic head phantom, respectively. It can be observed that the edges in the image reconstructed by FDK from the PWLS processed projection image are blurred compared with the image reconstructed by the PWLS using the anisotropic quadratic penalty. For a quantitative comparison, we calculated the MTF and noise level of the image of CTP591 module. The MTF curve was plotted in Fig. 5 and the standard deviation around the uniform region was 0.74 $\times 10^{-3}$. The MTF curves in Fig. 5 show that PWLS image reconstruction using the anisotropic quadratic penalty produces better image resolution at the matched noise level. This initial comparison study indicates that the edge-preserving penalty in the image domain produces higher image resolution than the same penalty applied in the projection domain because better edge definition is in the image domain than the projection domain.

In this work, our effort was focused on the noise suppression of CBCT using the iterative reconstruction algorithm. The presented iterative reconstruction algorithm can also be used to improve image quality of the 4D-CBCT.[36,37] In 4D-CBCT, projection views for a specific phase are usually irregular and undersampled. Direct reconstruction using the

conventional FDK algorithm from phase-binned projection data may lead to unacceptable results due to view aliasing artifacts. Several strategies, such as using slow-rotating imager[37] and interphase motion model,[38,39] have been proposed to enhance the image quality of 4D-CBCT. Iterative reconstruction algorithms incorporate both data acquisition geometry and sampling of projection views into the projection matrix automatically. Consequently, the quality of the CBCT image so obtained is generally superior over that reconstructed using an analytical method.[40]

Although iterative reconstruction algorithms have shown advantages for CT imaging in terms of noise suppression and structure preservation, computational time could be a challenge for its practical use. In our implementation, we computed the projection matrix A before iterative reconstruction. The projection matrix was stored as a file and served as a lookup table during iterations. It takes about 15 min to finish one iteration to reconstruct the CBCT images of a size $350 \times 350 \times 16$ using a PC with 3 GHz CPU. Nevertheless, the reconstruction can be sped up by graphics card acceleration[19,41] and parallel computation using PC clusters[42] and cell broadband engine.[18]

V. CONCLUSION

In this work, we presented a statistics-based iterative reconstruction algorithm for CBCT. The objective function was based on the PWLS criterion. To preserve edges in the reconstructed images, an anisotropic quadratic penalty was proposed. Noise and artifacts in low-dose CBCT are greatly suppressed using the presented PWLS reconstruction algorithm. Comparison studies with reconstruction based on the isotropic penalty have clearly shown the benefit of the proposed approach. The statistical iterative reconstruction algorithm significantly improves low-dose CBCT image quality and may find useful clinical applications in the future.

ACKNOWLEDGMENTS

APPENDIX: IMAGE RECONSTRUCTION ALGORITHM

The task for image reconstruction is to estimate the attenuation coefficient distribution map μ from the projection data $\hat{p}$ by minimizing Eq. (2). In this study, the minimization was performed iteratively using the Gauss–Seidel update algorithm, similar to that in Ref. 25,

Initialization:
$$\hat{\mu} = \text{FDK}\{\hat{p}\}$$
$$\hat{r} = \hat{y} - A\hat{\mu}$$
$$\Sigma = \text{diag}\{\sigma_i^2(p_i)\} = \text{diag}\{\exp(p_i)/N_{io}\}$$
$$s_j = a_j' \Sigma^{-1} a_j, \ \forall j,$$
$$w'_{jm} = w_{jm} \exp\left[-\left(\frac{\mu_j - \mu_m}{\delta}\right)^2\right], \ m \in N_j$$

For each iteration: (A1)
begin
  For each pixel j:
  begin
  $$\hat{\mu}_j^{old} := \hat{\mu}_j$$
  $$\alpha_j := s_j + \beta \Sigma_{m \in N_j} w'_{jm}$$
  $$\hat{\mu}_j^{new} := \frac{a_j' \Sigma^{-1} \hat{r} + s_j \hat{\mu}_j^{old} + \beta \Sigma_{m \in N_j} w'_{jm} \hat{\mu}_m}{\alpha_j}$$
  $$\hat{\mu}_j := \max\{0, \hat{\mu}_j^{new}\}$$
  $$\hat{r} := \hat{r} + a_j(\hat{\mu}_j^{old} - \hat{\mu}_j)$$
  $$w'_{jm} = w_{jm} \exp\left[-\left(\frac{\mu_j - \mu_m}{\delta}\right)^2\right], \ m \in N_j$$
  end
end

The iterations can be stopped by setting a threshold for the change of objective function or the number of iterations. In all of cases presented in this work, we stopped the computation at 20 iterations at which good convergence was seen through the observation of the reconstructed image at each iteration.

[a] Author to whom correspondence should be addressed. Present address: Department of Radiation Oncology, Stanford University School of Medicine, Clinical Cancer Center, 875 Blake Wilbur Drive, Rm CC-G204, Stanford, CA 94305-5847. Telephone: (650) 498-7896; Fax: (650) 498-4015. Electronic mail: lei@reyes.stanford.edu

[1] D. A. Jaffray, J. H. Siewerdsen, J. W. Wong, and A. A. Martinez, "Flat-panel cone-beam computed tomography for image-guided radiation therapy," Int. J. Radiat. Oncol., Biol., Phys. **53**, 1337–1349 (2002).

[2] L. Lee, Q. T. Le, and L. Xing, "Retrospective IMRT dose reconstruction based on cone-beam CT and MLC log-file," Int. J. Radiat. Oncol., Biol., Phys. **70**, 634–644 (2008).

[3] M. K. Islam, T. G. Purdie, B. D. Norrlinger, H. Alasti, D. J. Moseley, M. B. Sharpe, J. H. Siewerdsen, and D. A. Jaffray, "Patient dose from kilovoltage cone beam computed tomography imaging in radiation therapy," Med. Phys. **33**, 1573–1582 (2006).

[4] N. Wen, H. Q. Guan, R. Hammoud, D. Pradhan, T. Nurushev, S. D. Li, and B. Movsas, "Dose delivered from Varian's CBCT to patients receiving IMRT for prostate cancer," Phys. Med. Biol. **52**, 2267–2276 (2007).

[5] J. Hsieh, "Adaptive streak artifact reduction in computed tomography resulting from excessive x-ray photon noise," Med. Phys. **25**, 2139–2147 (1998).

[6] M. Kachelriess, O. Watzke, and W. A. Kalender, "Generalized multi-dimensional adaptive filtering for conventional and spiral single-slice, multi-slice, and cone-beam CT," Med. Phys. **28**, 475–490 (2001).

[7] T. F. Li, X. Li, J. Wang, J. H. Wen, H. B. Lu, J. Hsieh, and Z. R. Liang, "Nonlinear sinogram smoothing for low-dose x-ray CT," IEEE Trans. Nucl. Sci. **51**, 2505–2513 (2004).

[8] J. Wang, H. B. Lu, Z. R. Liang, D. Eremina, G. X. Zhang, S. Wang, J. Chen, and J. Manzione, "An experimental study on the noise properties of x-ray CT sinogram data in Radon space," Phys. Med. Biol. **53**, 3327–3341 (2008).

[9] A. R. Depierro, "A modified expectation maximization algorithm for penalized likelihood estimation in emission tomography," IEEE Trans. Med. Imaging **14**, 132–137 (1995).

[10] R. M. Leahy and J. Y. Qi, "Statistical approaches in quantitative positron emission tomography," Stat. Comput. **10**, 147–165 (2000).

[11] J. A. Fessler and A. O. Hero, "Penalized maximum-likelihood image-reconstruction using space-alternating generalized em algorithms," IEEE

Trans. Image Process. **4**, 1417–1429 (1995).

[12] T. Li, B. Thorndyke, E. Schreibmann, Y. Yang, and L. Xing, "Model-based image reconstruction for four-dimensional PET," Med. Phys. **33**, 1288–1298 (2006).

[13] F. J. Beekman and C. Kamphuis, "Ordered subset reconstruction for x-ray CT," Phys. Med. Biol. **46**, 1835–1844 (2001).

[14] H. Erdogan and J. A. Fessler, "Ordered subsets algorithms for transmission tomography," Phys. Med. Biol. **44**, 2835–2851 (1999).

[15] J. Nuyts, B. De Man, P. Dupont, M. Defrise, P. Suetens, and L. Mortelmans, "Iterative reconstruction for helical CT: A simulation study," Phys. Med. Biol. **43**, 729–737 (1998).

[16] K. Sauer and C. Bouman, "A local update strategy for iterative reconstruction from projections," IEEE Trans. Signal Process. **41**, 534–548 (1993).

[17] J. Wang, T. Li, H. B. Lu, and Z. R. Liang, "Penalized weighted least-squares approach to sinogram noise reduction and image reconstruction for low-dose x-ray computed tomography," IEEE Trans. Med. Imaging **25**, 1272–1283 (2006).

[18] M. Knaup, W. A. Kalender, and M. Kachelrieb, "Statistical cone-beam CT image reconstruction using the cell broadband engine," IEEE Nuclear Science Symposium Conference Record **5**, 2837–2840 (2006).

[19] F. Xu and K. Mueller, "Accelerating popular tomographic reconstruction algorithms on commodity PC graphics hardware," IEEE Trans. Nucl. Sci. **52**, 654–663 (2005).

[20] J. B. Thibault, K. D. Sauer, C. A. Bouman, and J. Hsieh, "A three-dimensional statistical approach to improved image quality for multislice helical CT," Med. Phys. **34**, 4526–4544 (2007).

[21] J. Song, Q. H. Liu, G. A. Johnson, and C. T. Badea, "Sparseness prior based iterative image reconstruction for retrospectively gated cardiac micro-CT," Med. Phys. **34**, 4476–4483 (2007).

[22] B. R. Whiting, P. Massoumzadeh, O. A. Earl, J. A. O'Sullivan, D. L. Snyder, and J. F. Williamson, "Properties of preprocessed sinogram data in x-ray computed tomography," Med. Phys. **33**, 3290–3303 (2006).

[23] P. Sukovic and N. H. Clinthorne, "Penalized weighted least-squares image reconstruction for dual energy x-ray transmission tomography," IEEE Trans. Med. Imaging **19**, 1075–1081 (2000).

[24] P. J. La Riviere, J. G. Bian, and P. A. Vargas, "Penalized-likelihood sinogram restoration for computed tomography," IEEE Trans. Med. Imaging **25**, 1022–1036 (2006).

[25] J. A. Fessler, "Penalized weighted least-squares image-reconstruction for positron emission tomography," IEEE Trans. Med. Imaging **13**, 290–300 (1994).

[26] I. A. Elbakri and J. A. Fessler, "Statistical image reconstruction for poly-energetic x-ray computed tomography," IEEE Trans. Med. Imaging **21**, 89–99 (2002).

[27] W. Chlewicki, F. Hermansen, and S. B. Hansen, "Noise reduction and convergence of Bayesian algorithms with blobs based on the Huber function and median root prior," Phys. Med. Biol. **49**, 4717–4730 (2004).

[28] S. Geman and D. Geman, "Stochastic relaxation, Gibbs distributions, and the Bayesian restoration of images," IEEE Trans. Pattern Anal. Mach. Intell. **6**, 721–741 (1984).

[29] D. Geman and G. Reynolds, "Constrained restoration and the recovery of discontinuities," IEEE Trans. Pattern Anal. Mach. Intell. **14**, 367–383 (1992).

[30] P. Charbonnier, L. BlancFeraud, G. Aubert, and M. Barlaud, "Deterministic edge-preserving regularization in computed imaging," IEEE Trans. Image Process. **6**, 298–311 (1997).

[31] G. Han, Z. Liang, and J. You, "A fast ray-tracing technique for TCT and ECT studies," IEEE Nuclear Science Symposium Conference Record **3**, 1515–1518 (1999).

[32] P. Perona and J. Malik, "Scale-space and edge-detection using anisotropic diffusion," IEEE Trans. Pattern Anal **12**, 629–639 (1990).

[33] E. Schreibmann, B. Thorndyke, T. Li, J. Wang, and L. Xing, "Four-dimensional image registration for IGRT," Int. J. Radiat. Oncol., Biol., Phys. **71**, 578–586 (2008).

[34] J. Wang, T. Li, Z. Liang, and L. Xing, "Dose reduction for kilovoltage cone-beam computed tomography in radiation therapy," Phys. Med. Biol. **53**, 2897–2909 (2008).

[35] P. J. La Riviere and P. Vargas, "Potential equivalence of sinogram and image-domain penalized likelihood methods," IEEE Nuclear Science Symposium Conference Record, 2007, NSS '07, 6, 4169–4173 (2007).

[36] T. Li, L. Xing, P. Munro, C. McGuinness, M. Chao, Y. Yang, B. Loo, and A. Koong, "Four-dimensional cone-beam computed tomography using an on-board imager," Med. Phys. **33**, 3825–3833 (2006).

[37] T. Li and L. Xing, "Optimizing 4D cone-beam CT acquisition protocol for external beam radiotherapy," Int. J. Radiat. Oncol., Biol., Phys. **67**, 1211–1219 (2007).

[38] R. Zeng, J. A. Fessler, and J. M. Balter, "Estimating 3-D respiratory motion from orbiting views by tomographic image registration," IEEE Trans. Med. Imaging **26**, 153–163 (2007).

[39] T. Li, A. Koong, and L. Xing, "Enhanced 4D cone-beam CT with inter-phase motion model," Med. Phys. **34**, 3688–3695 (2007).

[40] G.-H. Chen, J. Tang, and S. Leng, "Prior image constrained compressed sensing (PICCS): A method to accurately reconstruct dynamic CT images from highly undersampled projection data sets," Med. Phys. **35**, 660–663 (2008).

[41] Z. Wang, G. Han, T. Li, and Z. Liang, "Speedup OS-EM image reconstruction by PC graphics card technologies for quantitative SPECT with varying focal-length fan-beam collimation," IEEE Trans. Nucl. Sci. **52**, 1274–1280 (2005).

[42] X. Li, J. Ni, and G. Wang, "Parallel iterative cone-beam CT image reconstruction on a PC cluster," J. X-Ray Sci. Technol. **13**, 63–72 (2005).